Control of chiral orbital currents in a colossal magnetoresistance material

https://doi.org/10.1038/s41586-022-05262-3

Received: 8 June 2022

Accepted: 22 August 2022

Published online: 12 October 2022

Check for updates

Yu Zhang[1], Yifei Ni[1], Hengdi Zhao[1], Sami Hakani[2], Feng Ye[3], Lance DeLong[4], Itamar Kimchi[2]✉ & Gang Cao[1]✉

Colossal magnetoresistance (CMR) is an extraordinary enhancement of the electrical conductivity in the presence of a magnetic field. It is conventionally associated with a field-induced spin polarization that drastically reduces spin scattering and electric resistance. Ferrimagnetic $Mn_3Si_2Te_6$ is an intriguing exception to this rule: it exhibits a seven-order-of-magnitude reduction in *ab* plane resistivity that occurs only when a magnetic polarization is avoided[1,2]. Here, we report an exotic quantum state that is driven by *ab* plane chiral orbital currents (COC) flowing along edges of $MnTe_6$ octahedra. The *c* axis orbital moments of *ab* plane COC couple to the ferrimagnetic Mn spins to drastically increase the *ab* plane conductivity (CMR) when an external magnetic field is aligned along the magnetic hard *c* axis. Consequently, COC-driven CMR is highly susceptible to small direct currents exceeding a critical threshold, and can induce a time-dependent, bistable switching that mimics a first-order 'melting transition' that is a hallmark of the COC state. The demonstrated current-control of COC-enabled CMR offers a new paradigm for quantum technologies.

A necessary characteristic of all known CMR materials is an alignment of magnetic spins that drastically reduces electron scattering and/or band gaps, and thus electric resistance[3–11]. $Mn_3Si_2Te_6$ is unique, in that the *ab* plane resistivity ρ_a is reduced by up to seven orders of magnitude only when a magnetic field, *H*, is applied along the magnetic hard *c* axis or when a saturated magnetic state is absent[1]. By contrast, ρ_a decreases by no more than 20% when the magnetization is saturated by fields aligned with the magnetic easy *a* axis (or *ab* plane) (Fig. 1a,b). The data in Fig. 1b also show a large anisotropy field of at least 13 T, which is highly intriguing because magnetic anisotropy is a result of spin-orbit coupling, whereas the orbital angular momentum is zero for the Mn^{2+} ($3d^5$) ion in $Mn_3Si_2Te_6$. This new type of CMR has been confirmed[2], and signals the existence of a new quantum state yet to be identified and understood.

Herein we show that such a new state can be defined by its unconventional CMR, anisotropy and extraordinary response to application of small direct current (d.c.), *I*, including a first-order transition with bistable switching. The switching consists of an abrupt jump in voltage, *V*, which takes seconds or minutes to complete after application of a small current to the sample without further stimulus. The unusual time delay and voltage jump are strongly enhanced when *H* is oriented along the magnetic hard *c* axis (which favours CMR[1]) but are otherwise absent. Application of $H \parallel c$ axis also induces a surprising d.c. tunnelling behaviour that features $\Delta V/\Delta I = 0$. In short, the new state is highly conducting (CMR) and resilient when $H \parallel c$ axis, but is insulating and 'melts' (mimicking a solid-to-liquid phase transition) via a first-order, bistable switching when a small current exceeding a certain threshold is applied.

Taken separately, each key phenomenon (that is, CMR, anisotropy and bistable switching) defies conventional wisdom and models; the simultaneous occurrence of all these phenomena indicates that a new paradigm is required to understand the underlying state. Here, we argue all these exotic phenomena can be explained in terms of intra-unit-cell, *ab* plane COC that generate net *c* axis orbital magnetic moments (M_{COC}) that couple with the ferrimagnetically ordered Mn spins (M_{Mn}) (Fig. 1d,e).

Below the Curie temperature $T_C = 78$ K, the *ab* plane COC circulate along Te–Te edges of the $MnTe_6$ octahedra, which produces net M_{COC} oriented primarily along the *c* axis (Fig. 1d). The M_{COC} arising from Te orbitals are necessarily coupled with M_{Mn}, giving rise to an unusual spin-orbit effect that explains the observed large anisotropy field (Fig. 1b). Therefore, the observed magnetization results from both M_{Mn} and M_{COC}, and application of $H \parallel c$ axis can thereby amplify the *ab* plane COC and M_{COC} that underpin the CMR. The COC state Ψ_C is exceedingly sensitive to application of small *I*, and converts to a trivial state Ψ_T via first-order, bistable switching when $I > 2$ mA. Coupling of the COC to the rigid-but-extended Te sublattice and M_{Mn} allows Ψ_C to remain metastable over long timescales set by the motion of Te atomic clusters (as opposed to only electrons/Mn spins, which respond on picosecond timescales[12]). Consequently, the bistable switching or melting of Ψ_C requires seconds or minutes to occur after application of a small *I* to the sample. Our observed *T*-*I*-*H* phase diagram (Fig. 1g) shows that Ψ_C exists underneath a boundary sheet in *T*-*I*-*H* space that expands with increasing $H \parallel c$ axis.

COC have been investigated in previous studies of high-T_C cuprates[13–20], iridates[21–23], Kagome superconductors and magnets[24–26], a Kagome metal with a transport signature of loop current in a charge-ordered phase[27] and moiré heterostructures[28–30]. However, no macroscopic transport phenomena attributed to COC that coexist

[1]Department of Physics, University of Colorado at Boulder, Boulder, CO, USA. [2]School of Physics, Georgia Institute of Technology, Atlanta, GA, USA. [3]Neutron Scattering Division, Oak Ridge National Lab, Oak Ridge, TN, USA. [4]Department of Physics and Astronomy, University of Kentucky, Lexington, KY, USA. ✉e-mail: ikimchi3@gatech.edu; gang.cao@colorado.edu

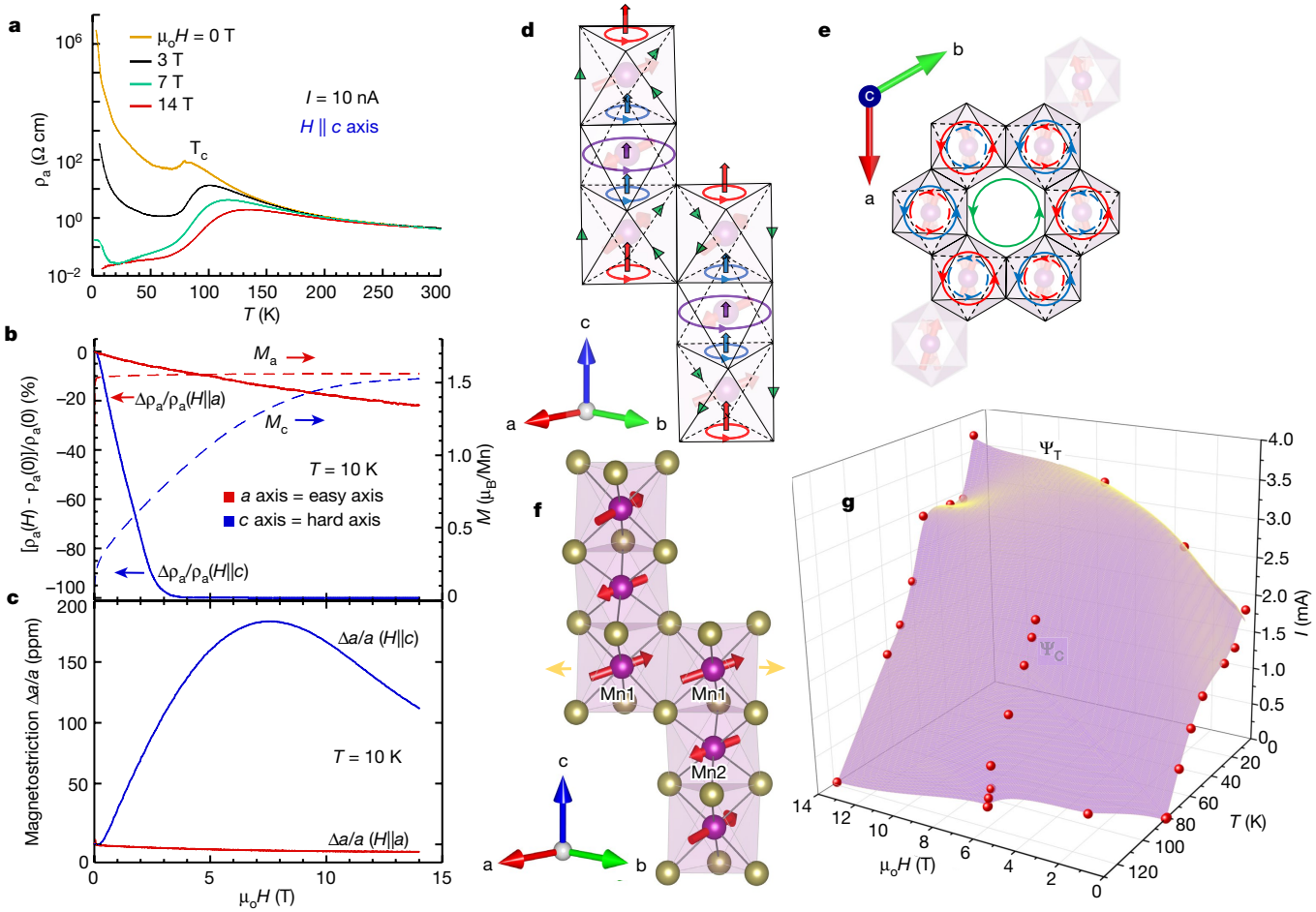

Fig. 1 | Physical properties in magnetic fields and phase diagram. **a**, Temperature dependence of a axis resistivity ρ_a at various magnetic fields (H). **b**, Magnetic field dependence of the a axis magnetoresistance ratio $(\rho_a(H) - \rho_a(0))/\rho_a(0)$ and the magnetization M (dashed lines, right scale) for $H \parallel c$ axis (blue) and $H \parallel a$ axis (red). **c**, a axis magnetostriction $\Delta a/a$ for $H \parallel c$ axis (blue) and $H \parallel a$ axis (red). **d**, COC and corresponding c axis M_{COC}; different colours indicate different magnitudes of M_{COC} (Fig. 4g and Extended Data Fig. 4). **e**, ab plane view of the COC. **f**, Crystal and magnetic structure; yellow arrows indicate ab plane expansion at $H \parallel c$ axis. **g**, T-I-H phase diagram. Note that $H \parallel c$ axis and $I \parallel a$ axis. Ψ_C exists under the purple sheet in the T-I-H space and beyond it is Ψ_T.

with a long-range magnetic order (as observed in this work) have been reported. The signature of COC coupled with long-range magnetic order can be particularly subtle because mirror and time-reversal symmetries are already broken; nevertheless, effects of COC can be exotic and strong, as demonstrated in this work.

$Mn_3Si_2Te_6$ forms a trimer-honeycomb lattice (Fig. 1e)[31,32] with a non-collinear magnetic structure in which the Mn spins lie predominantly within the ab plane (Fig. 1f). Our recent neutron study indicates that application of $H \parallel c$ axis causes a gradual tilting of the spins towards the c axis while retaining the underlying antiferromagnetic correlation along the c axis[33]. Such a large anisotropy in the CMR has been attributed to a spin-rotation driven metal–insulator transition[2]. In essence, an increasing c axis spin magnetization lifts the nodal-line band degeneracy and pushes one of the bands towards the Fermi surface, while the gap is preserved by the ab plane spin magnetization, yielding the large anisotropy[2]. However, like other CMR theories, this model depends on the c axis spin polarization. Therefore, the contrasting responses of the Mn spins and the CMR to $H \parallel c$ axis[1,2] emphasize an intriguing question: how can such an unusually small spin polarization result in the disproportionally enormous 10^7-CMR, which is also unusually current sensitive? Our conception of the COC state, as presented here, requires strong electron correlations and responds sensitively and strongly to $H \parallel c$ axis, which explains both the large magnitude and anisotropy of the CMR in $Mn_3Si_2Te_6$.

Physical properties in magnetic fields

The a axis resistivity ρ_a and the c axis resistivity ρ_c both rise rapidly below T_C (Fig. 1a)[1] (Extended Data Fig. 1a). The easy a axis magnetization M_a readily saturates to a value $M_s = 1.56\ \mu_B$/Mn for $\mu_o H_{\|a} > 0.05$ T (red dashed line in Fig. 1b). By contrast, the c axis magnetization M_c cannot fully attain the a axis value, even for $\mu_o H \geq 13$ T (blue dashed line in Fig. 1b)[1]. Such an unexpected anisotropy field suggests a new type of spin-orbit coupling is at play in $Mn_3Si_2Te_6$. Moreover, our measured average magnetic moments for Mn1 and Mn2 are 4.55 and 4.20 μ_B, respectively, considerably smaller than 5.0 μ_B anticipated for Mn^{2+} ($3d^5$)[33]. These data suggest a partial cancellation between M_{Mn} and M_{COC}; accordingly, we infer M_{COC} to be around 0.1 μ_B (Methods).

In addition, our magnetostriction data indicate that the a axis undergoes a significant expansion $\Delta a/a > 0$ when $H \parallel c$ axis but remains essentially unchanged when $H \parallel a$ axis (Fig. 1c); this indicates that a strong c axis magnetoelastic coupling favours an increase of orbital area associated with the COC (Extended Data Fig. 1b,c; Methods), as discussed below.

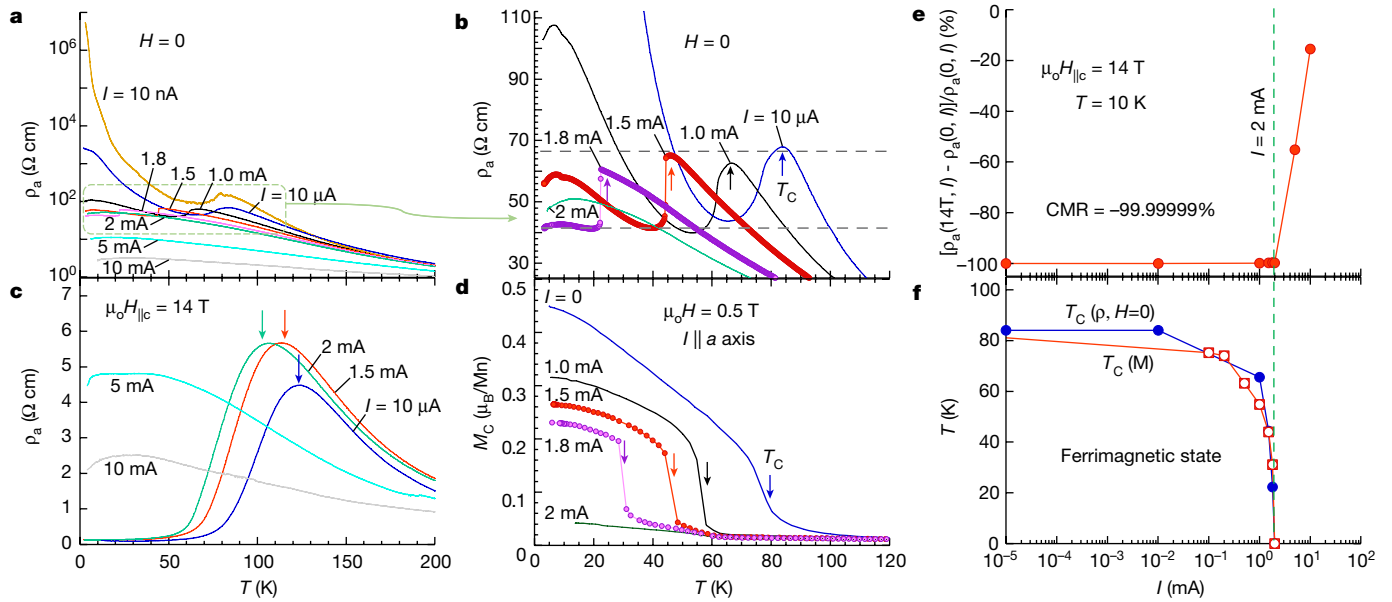

Fig. 2 | Response of physical properties to d.c. currents and magnetic fields. a, *a* axis resistivity ρ_a at various applied d.c. currents *I* for $H = 0$. **b**, Enlarged plot of ρ_a in the outlined region in **a**. Dashed grey lines highlight the near-constant values of ρ_a at and just below T_C. **c**, Temperature dependence of ρ_a at various applied d.c. currents *I* for $\mu_o H = 14$ T. Note that the CMR is absent for $I = 5$ mA and 10 mA. **d**, *c* axis magnetization M_c at various d.c. currents *I* along the *a* axis for $\mu_o H = 0.5$ T. Note the first-order transition evident in the ρ_a and M_c data induced by $I = 1.5$ and 1.8 mA. **e**, Change in ρ_a for $\mu_o H = 14$ T and various values of applied *I*. **f**, T_C at various values of *I* (generated from data in **b** and **d**). Note that both the CMR and T_C vanish for $I > 2$ mA.

Properties with small currents

ρ_a at $H = 0$ is reduced by up to six orders of magnitude when *I* is increased from 10 nA to 10 mA at low temperatures (Fig. 2a). T_C decreases rapidly with increasing $I \| a$ axis (Fig. 2b). Specifically, T_C decreases strongly from 83 K at 10 μA to 22 K at 1.8 mA, and eventually vanishes at 2 mA (Fig. 2b). M_c behaves similarly with increasing $I \| a$ axis (Fig. 2d). The signature of T_C evolves into a sharper, first-order transition with increasing *I*, until magnetic order is suppressed abruptly for $I \geq 2$ mA. Note the magnitude of ρ_a in the vicinity of T_C remains essentially unchanged (Fig. 2b). This remarkable behaviour suggests small currents (<2 mA) barely affect spin scattering of electrons near T_C, but weaken the spin exchange coupling that drives

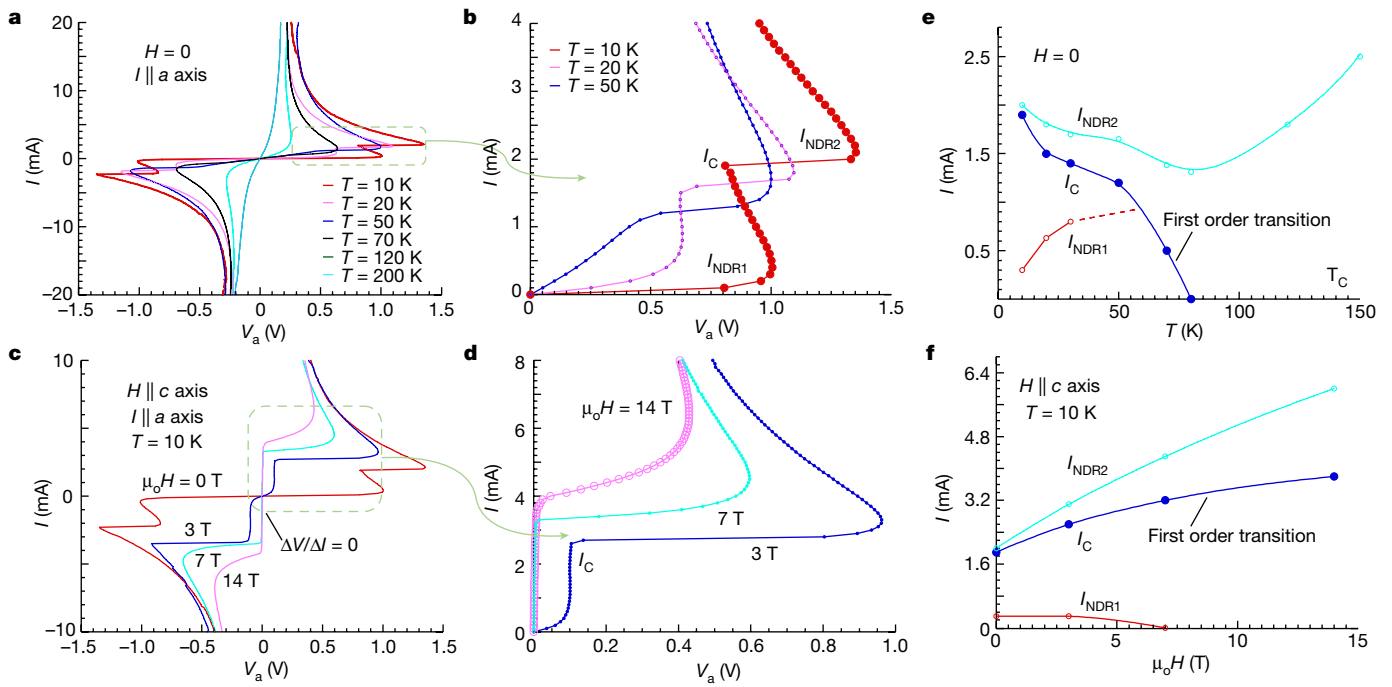

Fig. 3 | *a* axis *I*–*V* characteristic. a, At various temperatures and $H = 0$. **b**, Details of the outlined area in **a**; note the first-order transition at I_C. Note that the sudden voltage increase, $\Delta V = V_{NDR2} - V_C = 0.52$ V, results from a tiny current increase of 0.1 mA from the value of I_C. **c**, *I*–*V* characteristics for $T = 10$ K and $H \| c$ axis. **d**, Details of the outlined area in **c**. Note the regime where $\Delta V/\Delta I = 0$ emerges for $\mu_o H \geq 3$ T, and where V_a is approximately 0 for $I < I_C$ for $\mu_o H = 7$ and 14 T, and increasing *H* leads to an expansion of the region of $\Delta V/\Delta I = 0$. **e**,**f**, The critical current I_C as well as I_{NDR1} and I_{NDR2} as a function of temperature (**e**) and magnetic field (**f**). Note that I_C is depressed with increasing temperature and eventually vanishes near T_C but is enhanced and remains sharp with increasing $H \| c$ axis.

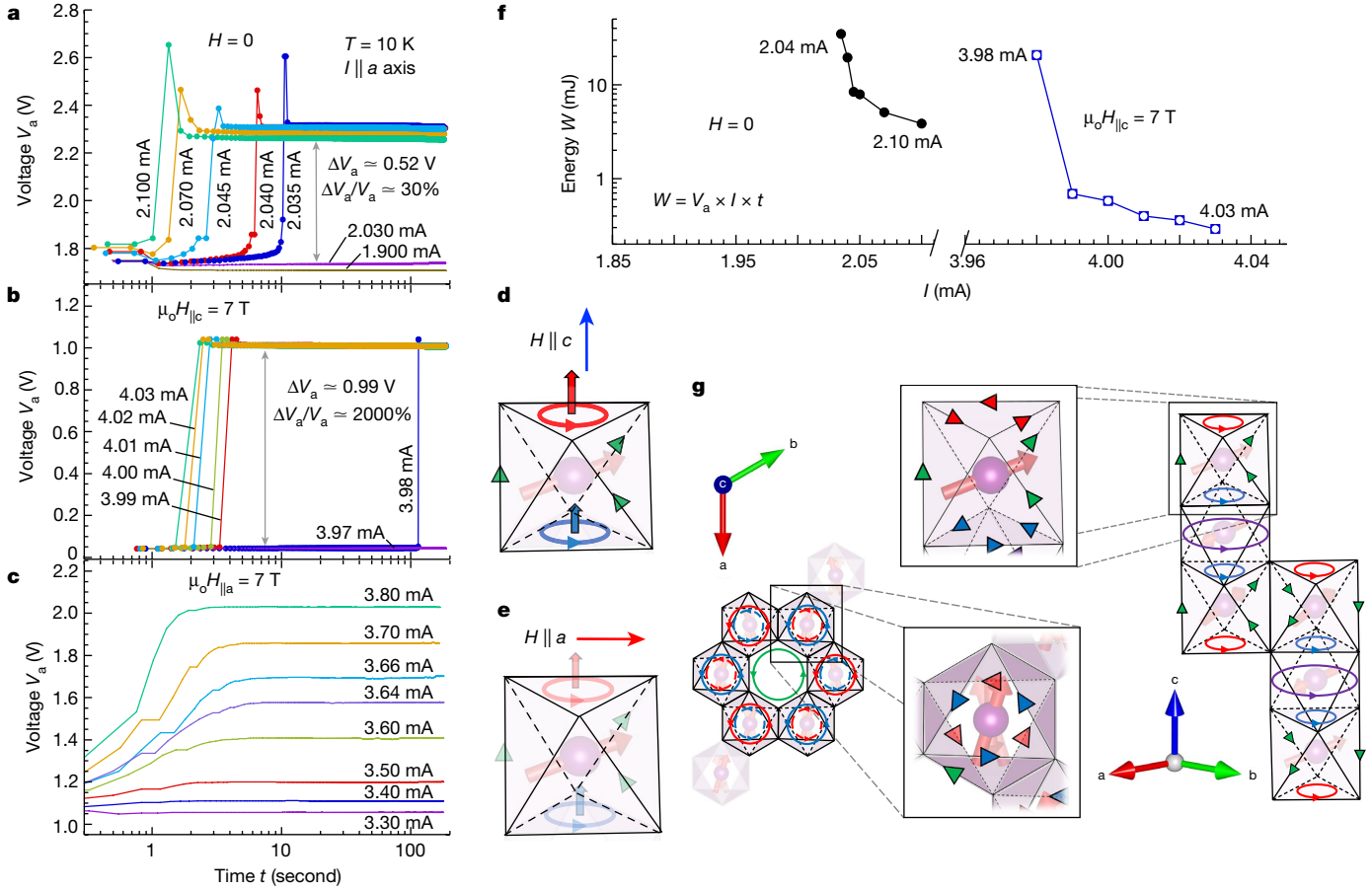

Fig. 4 | Time-dependent bistable switching and the COC. a–c, *a* axis voltage V_a as a function of time *t* at *T* = 10 K for *H* = 0 (**a**), $\mu_o H_{||c}$ = 7 T (**b**), and $\mu_o H_{||a}$ = 7 T (**c**). **d**,**e**, Schematics for *H* || *c* axis (**d**), which couples to and enhances Ψ_C, corresponding to the case in **b**, and *H* || *a* axis (**e**), which suppresses Ψ_C, corresponding to the case shown in **c**. Note that the *c* axis M_{COC} are denoted by the small red and blue arrows in the octahedron. **f**, The electric energy $W = V_a \times I \times t$ as a function of *I*. Note that *W* decreases with increasing *I*. **g**, Four-parameter, net nonzero *c* axis magnetization. The red, cylindrical arrows are the Mn spins. Four COC are denoted by small arrows (red, blue, green and purple). The top view of the Mn1 plane (left) and the side view (right) (Extended Data Fig. 4; Methods).

T_C, which differs markedly from other systems[34,35]. By contrast, T_C shifts systematically to higher temperatures with increasing *H* || *c* axis (Fig. 1a).

Properties in fields and with currents

The response of ρ_a to *I* changes drastically when *H* || *c* axis (Fig. 2c), which restores the magnetic order otherwise suppressed by *I*, and simultaneously reduces ρ_a, leading to a metallic state below T_C for $I \leq 2$ mA. However, for $I > 2$ mA, *H* reduces ρ_a only slightly, leaving a much weaker conducting state; the CMR is thus no longer present for *I* = 5 and 10 mA, despite the large $\mu_o H_{||c}$ = 14 T.

Combining the data for $\rho_a(H = 0, I)$ in Fig. 2a and $\rho_a(H_{||c} = 14\ T, I)$ in Fig. 2c yields the magnetoresistance ratio as a function of *I*, $(\rho_a(14\ T, I) - \rho_a(0, I))/\rho_a(0, I)$ at 10 K in Fig. 2e. Clearly, the CMR occurs only when $I \leq 2$ mA and abruptly disappears when $I > 2$ mA, which closely tracks the current dependence of T_C in Fig. 2f. While *H* || *c* axis enables the CMR, $I > 2$ mA weakens and eventually suppresses the ferrimagnetic state, thereby recovering the Ψ_T state without the CMR. The susceptibility to *I* highlights the unique CMR and is even more evident in the *I*–*V* characteristics.

Anomalous *I*–*V* characteristic

The *I*–*V* characteristic for H = 0 exhibits a first-order transition characterized by a critical current I_C that separates two distinct states. In addition, there are two onsets of S-shaped negative differential resistance (NDR)[36,37], I_{NDR1} ($< I_C$) and I_{NDR2} ($> I_C$) (Fig. 3a,b). The *I*–*V* curve bends over at an onset of the first NDR regime at $I = I_{NDR1}$, above which an increase in *I* leads to a decrease in *V*. This first NDR1 regime ends at I_C = 1.90 mA, where an abrupt increase in *V* occurs, indicating a first-order transition (Fig. 3b). This transition at I_C is followed by the second onset of NDR at $I = I_{NDR2}$ (Extended Data Fig. 2).

The magnetic field dependence of the *I*–*V* characteristic illustrates a new type of bistable switching (Fig. 3c). Upon the vanishing of I_{NDR1} at $\mu_o H_{||c} > 3$ T, an extraordinary region emerges with $\Delta V/\Delta I = 0$ for $0 \leq I \leq I_C$ (Fig. 3d). Note that at 7 T and 14 T, $V \approx 0$ as *I* increases from zero to I_C, a behaviour strikingly similar to the d.c. Josephson effect[38] although no superconducting state is involved here. This region disappears via an abrupt transition at I_C, and a more resistive state emerges at I_{NDR2} (Fig. 3d). The phase diagrams in Fig. 3e,f indicate that the first-order transition occurs at I_C as a function of temperature or magnetic field, respectively. Note that I_C behaves differently when *H* || *a* axis (Extended Data Fig. 2a).

Time-dependent bistable switching

A particularly striking and unique feature of Ψ_C is that the first-order, bistable switching requires a finite time (for example, seconds or minutes) and occurs without extra stimulus. The *a* axis voltage V_a, measured as a function of time *t* at 10 K, is shown in Fig. 4a–c (Extended Data Fig. 3). Each measurement of V_a starts at $t \equiv 0$ when a constant *I* is applied

and continued until t = 180 s (or 1,800 s (Extended Data Fig. 3a)) has elapsed. For example, when $I \leq 2.030$ mA at $t = 0$, V_a remains essentially constant for the time of measurements. A current increase of merely 0.25% (that is, from 2.030 to 2.035 mA) causes V_a to spike abruptly at t = 9.6 s, with a voltage increase of $\Delta V_a = 0.52$ V, or $\Delta V_a/V_a = 30\%$, and then immediately stabilizes at a constant value (Fig. 4a). Further, slight increases of I progressively shorten the delay time, but the change in voltage ΔV_a remains essentially the same, at 0.52 V. This protocol indicates that only two discrete states exist, separated by a first-order switching that persists up to T_C (Extended Data Fig. 3b). On the other hand, when $H \,||\, c$ axis (Fig. 4b), switching takes up to 114 s to occur at a significantly higher I = 3.98 mA with $\mu_o H_{||c}$ = 7 T, but involves a much larger voltage increase ΔV_a of approximately 0.99 V or $\Delta V_a/V_a$ of approximately 2,000% (Fig. 4b). By contrast, the abrupt bistable switching completely vanishes when $H \,||\, a$ axis (Fig. 4c), and is replaced by a gradual, continuous change in V_a with I.

The stark contrast between data in Fig. 4b for $H \,||\, c$ axis and Fig. 4c for $H \,||\, a$ axis reinforces the following key points. First, application of $H \,||\, c$ axis apparently strengthens Ψ_C via the c axis M_{COC} (Fig. 4d), which interlocks rigidly with the Te sublattice and M_{Mn}. It therefore takes a stronger I and a longer t for the charge carriers to alter the configuration of multiple atoms involved in conductive pathways. Second, the fact that this switching is always achieved via a first-order transition further emphasizes that there are key differences in the extended current paths and orbitals involved in the two states. Conversely, application of $H \,||\, a$ axis, where the CMR is absent, tilts the c axis M_{COC} towards the a axis, which weakens Ψ_C (Fig. 4e). Note that the energy dissipated at each switching for $H = 0$ and $\mu_o H_{||c} = 7$ T decreases rapidly with increasing I, which is clearly inconsistent with Joule heating (Fig. 4f) (Methods).

Discussion and outlook

The COC, which couple to the ferrimagnetic state, originate from spontaneous breaking of time-reversal symmetry below T_C = 78 K and circulate along Te–Te edges of the $MnTe_6$ octahedra, producing M_{COC} oriented primarily along the c axis (Methods). (Note that similar orbital moments of loop currents in cuprates have been discussed, but with no net moment[19,39].) In the absence of $H \,||\, c$ axis, the net circulation of the COC is zero as the COC can circulate both clockwise and counterclockwise (Figs. 1d,e and 4g). This results in a complicated configuration of disordered circulation domains that cause strong scattering and high resistance. Application of $H \,||\, c$ axis favours only one circulation (that is, either clockwise or counterclockwise) and enlarges its domains (and concurrently reducing the domains with the opposite circulation). As the overall conductivity is a sensitive function of the configuration of the COC domains, the alignment of the dominant circulation domains is crucial for the enhancement of Ψ_C by $H \,||\, c$ axis, and the sharp reduction in electron scattering evident in the 10^7-CMR (Fig. 1a,b).

Applying a nonequilibrium current I > 2mA destabilizes Ψ_C in favour of Ψ_T as Ψ_C permits no net a axis current (Fig. 4g) (Extended Data Fig. 4; Methods). The resistivity is reduced with increased I, but at the same time, the increased I also weakens and eventually suppresses the ferrimagnetic state and, consequently, Ψ_C, leading to a first-order phase transition that destroys Ψ_C (Fig. 2a–d).

The rigid coupling of the COC (and M_{COC}) to the Te sublattice and M_{Mn} is a signature of Ψ_C. The COC extend over multiple atomic sites with couplings that depend on the ionic positions and dictate the current strength. Therefore, Ψ_C entails a particularly strong coupling between the lattice, the c axis M_{COC} and M_{Mn}, as well as the anisotropic magnetoelastic coupling manifest in the magnetostriction (Fig. 1c; Methods). Such a rigid coupling in Ψ_C explains the current-driven first-order transition from Ψ_C to Ψ_T. This coupling also enables Ψ_C to remain metastable over the long timescales that are set by Te atomic motion and bond lengths, or fluctuations/phonon effects.

Further probes (for example, optical control[40]) of Ψ_C, particularly the orbital magnetization and its response to $H \,||\, c$ axis, will yield more insights into the COC. For example, a Kerr or terahertz Kerr effect couples directly to electron current operators, but indirectly to spins via spin-orbit coupling[41]. A large, increasing Kerr effect with increasing $H \,||\, c$ axis would provide further evidence for the existence of a strongly correlated COC state in $Mn_3Si_2Te_6$.

Online content

Any methods, additional references, Nature Research reporting summaries, source data, extended data, supplementary information, acknowledgements, peer review information; details of author contributions and competing interests; and statements of data and code availability are available at https://doi.org/10.1038/s41586-022-05262-3.

1. Ni, Y. et al. Colossal magnetoresistance via avoiding fully polarized magnetization in the ferrimagnetic insulator $Mn_3Si_2Te_6$. *Phys. Rev. B* **103**, L161105 (2021).
2. Seo, J. et al. Colossal angular magnetoresistance in ferrimagnetic nodal-line semiconductors. *Nature* **599**, 576–581 (2021).
3. Ramirez, A. P. Colossal magnetoresistance. *J. Phys. Condens. Matter* **9**, 8171–8199 (1997).
4. Millis, A. J., Shraiman, B. I. & Mueller, R. Dynamic Jahn–Teller effect and colossal magnetoresistance in $La_{1-x}Sr_xMnO_3$. *Phys. Rev. Lett.* **77**, 175–178 (1996).
5. Salamon, M. B. & Jaime, M. The physics of manganites: structure and transport. *Rev. Mod. Phys.* **73**, 583 (2001).
6. Dagotto, E. *Nanoscale Phase Separation and Colossal Magnetoresistance* (Springer, 2002).
7. Tokura, Y. Critical features of colossal magnetoresistive manganites. *Rep. Prog. Phys.* **69**, 797–848 (2006).
8. Majumdar, P. & Littlewood, P. Magnetoresistance in Mn pyrochlore: electrical transport in a low carrier density ferromagnet. *Phys. Rev. Lett.* **81**, 1314–1317 (1998).
9. Shimakawa, Y., Kubo, Y. & Manako, T. Giant magnetoresistance in $Tl_2Mn_2O_7$ with the pyrochlore structure. *Nature* **379**, 53–55 (1996).
10. Rosa, P. et al. Colossal magnetoresistance in a nonsymmorphic antiferromagnetic insulator. *npj Quantum Mater.* **5**, 52 (2020).
11. Yin, J. et al. Large negative magnetoresistance in the antiferromagnetic rare-earth dichalcogenide, $EuTe_2$. *Phys. Rev. Mater.* **4**, 013405 (2020).
12. Perfetti, L. et al. Ultrafast electron relaxation in superconducting $Bi_2Sr_2CaCu_2O_{8+\delta}$ by time-resolved photoelectron spectroscopy. *Phys. Rev. Lett.* **99**, 197001 (2007).
13. Varma, C. M. Theory of the pseudogap state of the cuprates. *Phys. Rev. B* **73**, 155113 (2006).
14. Varma, C. M. Pseudogap in cuprates in the loop-current ordered state. *J. Phys. Condens. Matter* **26**, 505701 (2014).
15. Pershoguba, S. S., Kechedzhi, K. & Yakovenko, V. M. Proposed chiral texture of the magnetic moments of unit-cell loop currents in the pseudogap phase of cuprate superconductors. *Phys. Rev. Lett.* **111**, 047005 (2013).
16. Pershoguba, S. S., Kechedzhi, K. & Yakovenko, V. M. Erratum: proposed chiral texture of the magnetic moments of unit-cell loop currents in the pseudogap phase of cuprate. *Phys. Rev. Lett.* **113**, 129901 (2014).
17. Scagnoli, V. et al. Observation of orbital currents in CuO. *Science* **332**, 696–698 (2011).
18. Di Matteo, S. & Norman, M. R. Orbital currents, anapoles, and magnetic quadrupoles in CuO. *Phys. Rev. B* **85**, 235143 (2012).
19. Yakovenko, V. M. Tilted loop currents in cuprate superconductors. *Physica B* **460**, 159–164 (2015).
20. Bourges, P., Bounoua, D. & Sidis, Y. Loop currents in quantum matter. *Comp. Rend. Phys.* **22**, 7–31 (2021).
21. Zhao, L. et al. Evidence of an odd-parity hidden order in a spin-orbit coupled correlated iridates. *Nat. Phys.* **12**, 32–36 (2015).
22. Jeong, J., Sidis, Y., Louat, A., Brouet, V. & Bourges, P. Time-reversal symmetry breaking hidden order in $Sr_2(Ir,Rh)O_4$. *Nat. Commun.* **8**, 15119 (2017).
23. Murayama, H. et al. Bond directional anapole order in a spin-orbit coupled mott insulator $Sr_2Ir_{1-x}Rh_xO_4$. *Phys. Rev. X* **11**, 011021 (2021).
24. Jiang, Y.-X. et al. Unconventional chiral charge order in kagome superconductor KV_3Sb_5. *Nat. Mater.* **20**, 1353–1357 (2021).
25. Feng, X., Jiang, K., Wang, Z. & Hu, J. Chiral flux phase in the Kagome superconductor AV_3Sb_5. *Sci. Bull.* **66**, 1384–1388 (2021).
26. Teng, X. et al. Discovery of charge density wave in a kagome lattice antiferromagnet. *Nature* **609**, 490–495 (2022).
27. Guo, C. et al. Field-tuned chiral transport in charge-ordered CsV_3Sb_5. Preprint at https://arxiv.org/abs/2203.09593.
28. Serlin, M. et al. Intrinsic quantized anomalous Hall effect in a moiré heterostructure. *Science* **367**, 900–903 (2020).
29. Tschirhart, C. L. et al. Imaging orbital ferromagnetism in a moiré Chern insulator. *Science* **372**, 1323–1327 (2021).
30. Sharpe, A. L. et al. Emergent ferromagnetism near three-quarters filling in twisted bilayer graphene. *Science* **365**, 605–608 (2019).
31. May, A. F. et al. Magnetic order and interactions in ferrimagnetic $Mn_3Si_2Te_6$. *Phys. Rev. B* **95**, 174440 (2017).
32. Liu, Y. & Petrovic, C. Critical behavior and magnetocaloric effect in $Mn_3Si_2Te_6$. *Phys. Rev. B* **98**, 064423 (2018).
33. Ye, F. et al. Magnetic structure and spin fluctuation in colossal magnetoresistance ferrimagnet $Mn_3Si_2Te_6$. arXiv:2209.13664 (2022).

34. Cao, G. et al. Electrical control of structural and physical properties via strong spin-orbit interactions in Sr_2IrO_4. *Phys. Rev. Lett.* **120**, 017201 (2018).
35. Zhao, H. et al. Nonequilibrium orbital transitions via applied electrical current in calcium ruthenates. *Phys. Rev. B* **100**, 241104(R) (2019).
36. Jeong, D. S. et al. Emerging memories: resistive switching mechanisms and current status. *Rep. Prog. Phys.* **75**, 076502 (2012).
37. Meijer, G. I. Who wins the nonvolatile memory race? *Science* **319**, 1625–1626 (2008).
38. Giaever, I. & Megerle, K. Study of superconductors by electron tunneling. *Phys. Rev.* **122**, 1101–1111 (1961).
39. Tang, Y. et al. Orientation of the intra-unit-cell magnetic moment in the high-Tc superconductor $HgBa_2CuO_{4+\delta}$. *Phys. Rev. B* **98**, 214418 (2018).
40. Pershoguba, S. S. & Yakovenko, V. M. Optical control of topological memory based on orbital magnetization. *Phys. Rev. B* **105**, 064423 (2022).
41. Nandkishore, R. & Levitov, L. Polar Kerr effect and time reversal symmetry breaking in bilayer graphene. *Phys. Rev. Lett.* **107**, 097402 (2011).

Methods

Experimental details

Single crystals of $Mn_3Si_2Te_6$ were grown using a flux method. Measurements of crystal structures were performed using a Bruker Quest ECO single-crystal diffractometer with an Oxford Cryosystem providing sample temperature environments ranging from 80 K to 400 K. Chemical analyses of the samples were performed using a combination of a Hitachi MT3030 Plus Scanning Electron Microscope and an Oxford Energy Dispersive X-Ray Spectroscopy (EDX). The measurements of the electric resistivity and *I*–*V* characteristic were carried out using a Quantum Design (QD) Dynacool PPMS system having a 14-T magnet and a set of external Keithley meters that measure *I* and *V* with high precision. Magnetization measurements under applied electric current were performed using a QD MPMS-XL magnetometer with a home-made probe. The magnetostriction was measured using a home-made dilatometer compatible with the QD Dynacool PPMS system. The dilatometer consists of four identical KYOWA, type KFL strain gauges forming a Wheatstone bridge with the sample mounted on one arm. The other three strain gauges act as compensators to cancel unwanted shifts in the strain gauges due to changes in temperature and/or magnetic field.

Further notes on the COC, CMR, crystal structure and bistable switching

The COC not only coexist with the long-range magnetic order but also produce their own nonzero net magnetization. COC discussed in other materials involve zero net circulation and zero net magnetic moment. By their observed symmetries, they necessarily entail an 'antiferromagnetic' pattern of clockwise and counterclockwise COC circulations. This distinction is key to what makes the COC of $Mn_3Si_2Te_6$ unique.

It is important to note that CMR is described by a lowest-order tensor, unlike high-order, nonlinear electric response known as electronic magneto-chiral anisotropy.

$Mn_3Si_2Te_6$ crystallizes in a trigonal space group P-31c (no. 163) with two inequivalent Mn sites, Mn1 and Mn2, forming a trimer-honeycomb lattice (Fig. 1d,e). It orders ferrimagnetically at $T_C = 78$ K[31,32] with the Mn spins antiferromagnetically coupled along the *c* axis[1]. Our recent neutron diffraction data show a noncollinear magnetic structure below T_C, in which the Mn spins lie predominantly within the *ab* plane, but tilt within the *ab* plane and cant towards the *c* axis by 10° under ambient conditions (Fig. 1f).

Note that ρ_a of $Mn_3Si_2Te_6$ does not follow an activation law and or a simple power law at low temperatures (Extended Data Fig. 1a), which differs from that reported in Seo et al.[2].

The CMR is enhanced (Extended Data Fig. 1b), whereas the saturated magnetization M_s is reduced to 1.40 μ_B/Mn in $Mn_3(Si_{1-x}Ge_x)_2Te_6$ (Extended Data Fig. 1c), which is further evidence that larger orbital moments of the COC state partially cancel the net magnetic moments. On the other hand, in $Mn_3Si_2(Te_{1-y}Se_y)_6$ the CMR is weakened (Extended Data Fig. 1b), but M_s is enhanced up to 1.7 μ_B/Mn (Extended Data Fig. 1c), which indicates that smaller orbital moments lie on the mixed-occupancy, chalcogenide sublattice, resulting in a weaker cancellation effect. It is also noteworthy that the Ge doping that enhances the CMR also expands the *ab* plane, whereas Se doping that weakens the CMR shrinks the *ab* plane (inset in Extended Data Fig. 1b).

M_{COC} is estimated based on the total measured moments, 4.55 and 4.20 μ_B for Mn1 and Mn2, respectively[33], which are significantly smaller than the expected 5 μ_B. The reduced magnetic moments suggest partial cancellation between M_{Mn} and M_{COC}. We infer that the upper limit of M_{COC} is on the order of 0.10 μ_B. We are mindful that it is always possible that the Mn local moments could be smaller than expected, thus less cancellation with M_{COC} would be needed to produce the total observed moments.

The magnetostriction is associated with M_{COC} because the Lorentz force acts to expand an *ab* plane COC circulating on the rigid Te–Te edges of $MnTe_6$ octahedra when $H \parallel c$ axis. The net orbital magnetization, which equals the loop current times the orbital area, naturally increases due to increasing the orbital area. As such, the larger the orbital area or *ab* plane, the larger M_{COC} becomes; and a large M_{COC} renders a larger cancellation, thus a smaller total, observed moment. This also explains the inverse correlation between the CMR and M_s illustrated in Extended Data Fig. 1b,c, further highlighting the role of M_{COC}.

The rigid coupling of the COC to the Te sublattice and M_{Mn} is a signature of the new state. The COC extend over multiple atomic sites, with couplings that depend on the ionic positions and dictate the current strength. The strong coupling sets timescales that enable the COC state to remain metastable over seconds or minutes before undergoing a first-order transition to a trivial state when applied d.c. currents exceed certain critical values. Such a long timescale is rare, if not unprecedented. We infer that this transition may mimic a solid-to-liquid phase transition.

During solid melting, thermal energy is absorbed to break chemical bonds, without raising temperature. The temperature of the system rises abruptly only when all the bonds are broken, that is, the solid is completely melted. An analogy drawn here is that, during the COC melting, the applied d.c. currents circulate in the sample to break COC in every unit cell, without causing a voltage or resistance increase before all COC are completely melted. In any case, breaking the COC inevitably causes rearrangements of Te orbitals and, more generally, changing lattice properties and, consequently, a long delay for switching.

Further discussion on the COC

Below T_C, ferrimagnetic order is observed with a magnetic symmetry group *C2′/c′* (no. 15.89, BNS setting), which allows certain configurations of Te orbital currents circulating within the unit cell. As we are particularly interested in the COC configurations with *c* axis orbital moments, we focus on one subset of COC patterns that respect not only the magnetic group no. 15.89, but also the additional threefold rotational symmetry inherited from the full crystal space group P-31c (no. 163). There are four independent current patterns that preserve this combination of 15.89 plus threefold rotations. The resulting four-parameter COC state is depicted in Fig. 4g.

This symmetry-preserving COC state Ψ_C yields currents circulating on octahedral top/bottom faces as well as around Mn2 and Si sites. The resulting magnetic moments are all oriented exactly along the *c* axis, yielding a nonzero M_{COC}. There are four additional independent current patterns that preserve the magnetic group no. 15.89 but break threefold rotation symmetry; these patterns, denoted Ψ_a, are described below, and produce moments oriented within the *ab* plane, coupling only weakly to *c* axis fields. Henceforth, we focus on the Ψ_C state that makes the primary contribution to the COC state and its response to *c* axis fields.

The COC circulate along Te–Te octahedra edges and involve primarily Te orbitals. The Mn local moment pattern detected in neutron scattering linearly couples to the order parameter of Ψ_C in a Landau-Ginzburg theory. Therefore, the COC and localized moments both contribute to the observed magnetic pattern and cannot be fully distinguished. As such, Ψ_C can be viewed as a superposition of Mn and Te states that forms time-reversal-breaking multisite molecular orbitals.

Application of $H \parallel c$ axis couples to Ψ_C via the *c* axis orbital moments, which in turn drastically enhances the COC order parameter, therefore, the hopping matrix elements, and accommodates more current passing through the sample, leading to the observed CMR. Clearly, application of $H \parallel a$ axis weakens the *c* axis orbital moments, thus reducing Ψ_C, and necessarily causes suppression of the CMR. On the other hand, applying uniform current $I > 2$mA (along the *a* or *c* axes) weakens the COC order parameter, therefore destabilizing Ψ_C in favour of the trivial state Ψ_T. This is expected because the COC configuration does not permit any net current because each of the four independent parameters that specify Ψ_C forms a circulating current within the unit cell with no net uniform

component (Fig. 4g). The resistivity is reduced with increased I; but at the same time, the increased I also weakens and eventually suppresses the ferrimagnetic state and, consequently, Ψ_C, leading to a first-order phase transition that destroys the COC state (Fig. 2).

Strong electron-lattice coupling is an important feature of Ψ_C. The COC extend over multiple atomic sites, with couplings that depend on the ionic positions in the lattice and determine the current strengths. Therefore, Ψ_C entails a much stronger coupling between the lattice and the c axis magnetic moments, and associated anisotropic magnetoelastic coupling, compared with that due to conventional Mn^{+2}-site, spin-only moments. This property of Ψ_C is consistent with the large magnetostriction $\Delta a/a$ when $H \parallel c$ axis and the nearly negligible $\Delta a/a$ when $H \parallel a$ axis (Fig. 1c). Note that these effects occur only below T_C where Ψ_C exists.

The strong coupling of COC to the lattice suggests that the current-driven transition from Ψ_C to Ψ_T should be strongly first order as observed (Figs. 1–4). The long timescale (seconds or minutes) for the bistable switching is consistent with a picture wherein melting Ψ_C involves changing lattice properties, thus allowing Ψ_C to remain metastable over long timescales set by ionic motion rather than just by fast electrons and/or Mn spins. The coupling between Ψ_C and the lattice increases when $H \parallel c$ axis, thus the observed longer time delay, but significantly weakened when $H \parallel a$ axis, leading to a mixed state with coexisting Ψ_C and Ψ_T.

The full COC state is parametrized by eight independent COC. These include three of the COC of Ψ_C (red, blue and green in Fig. 4g) and the six COC shown in Extended Data Fig. 4 that do not constitute a linearly independent set of COC. One of the COC (purple in Fig. 4g) is in fact a linear combination of COC that circulate around Mn1 atoms (Extended Data Fig. 4a) and different COC from Ψ_C (blue in Fig. 4g).

The sum of the three COC circulating about Mn1 atoms (Extended Data Fig. 4(a)) in equal magnitudes in fact gives the difference of two COC of Ψ_C (red minus blue in Fig. 4g). Moreover, the sum of the three COC in equal magnitudes circulating about the Mn2 atoms (Extended Data Fig. 4b) gives another difference of two COC of Ψ_C (blue minus twice purple). These linear combinations are allowed by the threefold rotational symmetry described above. In total, the COC state thus has the four parameters of Ψ_C, six extra parameters symmetry allowed by the magnetic space group and two constraints relating the ten parameters. Indeed, the full COC state is thus parametrized by eight independent COC.

The unit vector normal to the plane about which each COC circulates in Ψ_C is exactly along the c axis. The COC of this state clearly couple most strongly to applied fields in the c axis. By contrast, the COC of Ψ_a do not couple strongly to applied fields in the c axis. Instead, the orbital moments generated by the COC in the Mn1 plane point primarily in the ab plane, and they are (approximately) pairwise separated by 120°. Their orientation is slightly nontrivial as the $MnTe_6$ octahedra are not regular octahedra. The orbital moments generated by the COC in the Mn2 plane similarly are not well aligned with the c axis, and their orientation is also nontrivial.

Absence of Joule heating

Self-heating effects cause a continuous drift in local temperature; these effects are generally isotropic or diffusive and vary continuously with changing current. Such behaviour is ruled out in the present study by (1) the abrupt nature of the switching without any drifting, (2) the independence of the two discrete values of V_a on the magnitude of I (Fig. 4a,b), (3) the extremely anisotropic behaviour in (see Fig. 4b,c) and, moreover, (4) the electric energy $W = V_a \times I \times t$ dissipated by the applied current at each switching, for $H = 0$ and $\mu_o H_{\parallel c} = 7$ T, decreases rapidly with increasing I, which is clearly inconsistent with Joule heating (Fig. 4f).

Data availability

The data that support the findings of this work are available from the corresponding authors upon request.

Acknowledgements G.C. thanks M. Lee, R. Nandkishore, X. Chen, M. Hermele, D. Singh, D. Reznik, D. Dessau and N. Clark for useful discussions. I.K. thanks E. Berg, M. Mourigal, B. Uchoa, C. Varma and Z. Wang for useful discussions. This work is supported by National Science Foundation via grants no. DMR 1903888 and DMR 2204811. The theoretical part of this work is in part performed at Aspen Center for Physics, which is supported by National Science Foundation grant PHY-1607611. The work at the Spallation Neutron Source at the Oak Ridge Natinoal Laboratory is sponsored by the Scientific User Facilities Division, Office of Basic Energy Sciences, US Department of Energy.

Author contributions Y.Z. conducted measurements of the physical properties and data analysis; Y.N. grew the single crystals, characterized the crystal structure of the crystals, measured magnetization with applied currents and contributed to the data analysis; H.Z. conducted measurements of crystal and physical properties including the magnetostriction and the data analysis; F.Y. determined the magnetic structure of $Mn_3Si_2Te_6$ using neutron diffraction and contributed to the data analysis; S.H. contributed to the theoretical analysis including detailed configurations of chiral orbital currents presented in the figures; L.D. contributed to the data analysis and paper writing; I.K. proposed the theoretical argument, formed the theoretical discussion and contributed to paper writing; G.C. initiated and directed this work, analyzed the data, constructed the figures and wrote the paper.

Competing interests The authors declare no competing interests.

Additional information
Supplementary information The online version contains supplementary material available at https://doi.org/10.1038/s41586-022-05262-3.
Correspondence and requests for materials should be addressed to Itamar Kimchi or Gang Cao.
Peer review information *Nature* thanks Lan Wang, Victor Yakovenko and Meng Wang for their contribution to the peer review of this work. Peer reviewer reports are available.

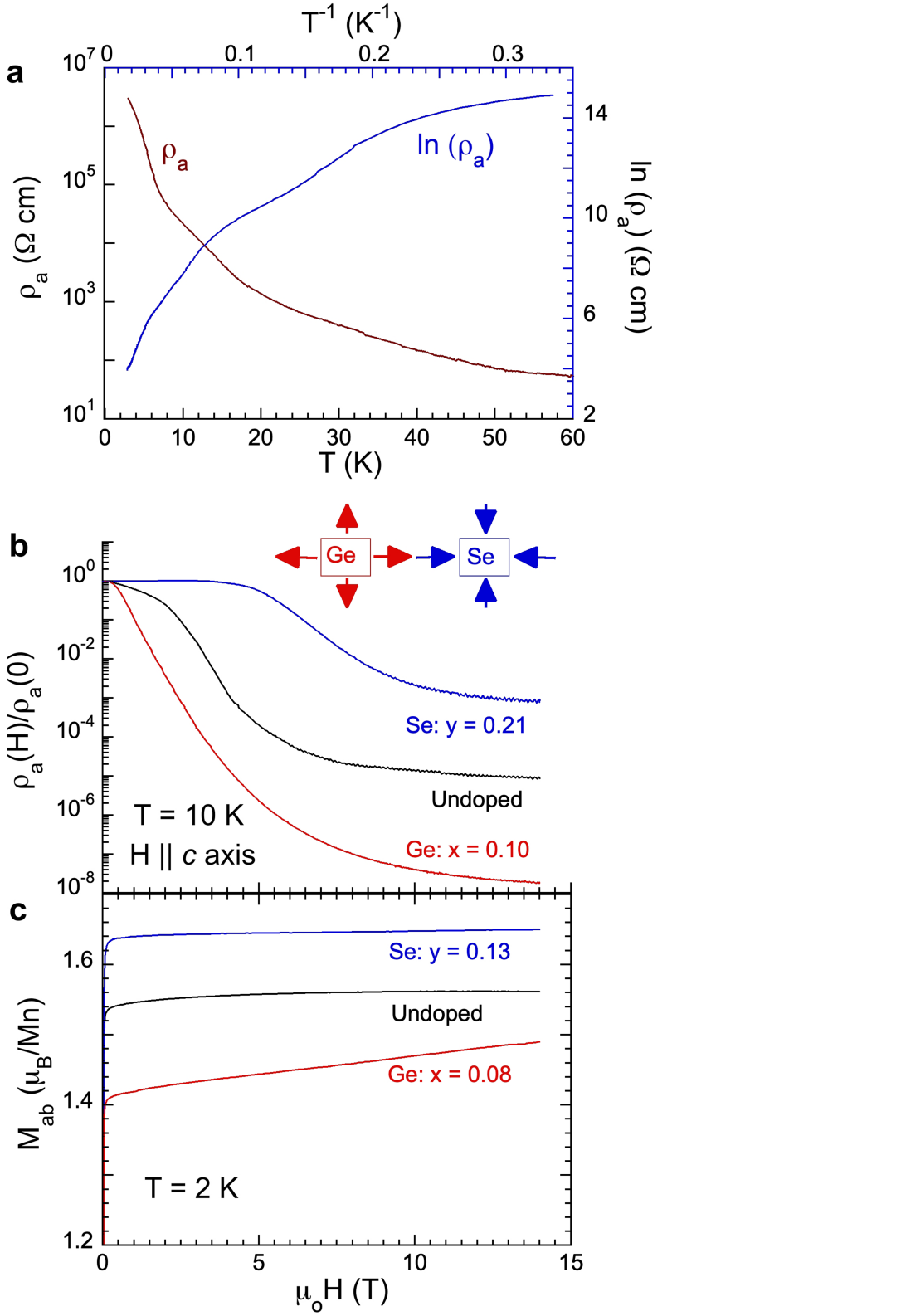

Extended Data Fig. 1 | Resistivity at low temperatures for $Mn_3Si_2Te_6$ and transport and magnetic properties for $Mn_3(Si_{1-x}Ge_x)_2Te_6$, $Mn_3Si_2(Te_{1-y}Se_y)_6$. **a**, The temperature dependence of the *a*-axis resistivity ρ_a at low temperatures (data in brown), and ln (ρ_a) versus T^{-1} (data in blue). Note that ρ_a does not follow an activation law and or a simple power law at low temperatures. **b**, **c**, The magnetic field dependence of the *a*-axis magnetoresistance ratio defined by $\rho_a(H)/\rho_a(0)$ (**b**) and the easy *a*-axis magnetization M_a (**c**) for $Mn_3(Si_{1-x}Ge_x)_2Te_6$ (red), $Mn_3Si_2(Te_{1-y}Se_y)_6$ (blue) and undoped compound (black), respectively. Inset in **b** schematic illustration of the unit cell expansion and contraction due to Ge doping (red) and Se doping (blue), respectively.

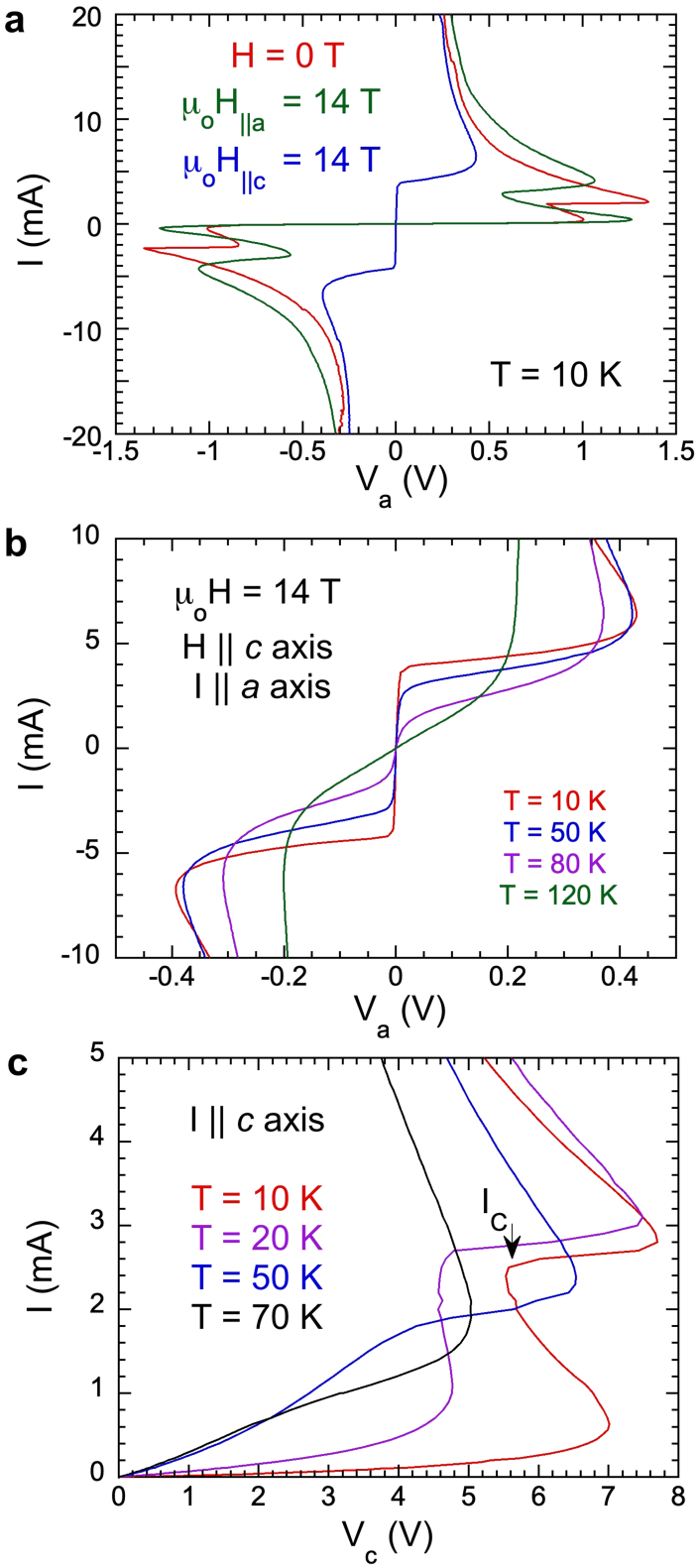

Extended Data Fig. 2 | Additional *I-V* characteristic. a, Comparison of the *I-V* characteristic at $H \| a$ axis and $H \| c$ axis: the *a*-axis *I-V* characteristic at 10 K for $H = 0$ (red), $\mu_0 H = 14$ T along the *a* axis (green) and the *c* axis (blue). Note that the regime where $\Delta V/\Delta I = 0$ emerges only when $H \| c$ axis. **b**, The *I-V* characteristic at $\mu_0 H_{\|c} = 14$ T for various temperatures. Note the regime $\Delta V/\Delta I = 0$ persists up to 70 K. **c**, The *I-V* characteristic at $I \| c$ axis for various temperatures. Note that the *I-V* characteristic is qualitatively similar to that for $I \| a$ axis but the first-order switching at I_c is weaker.

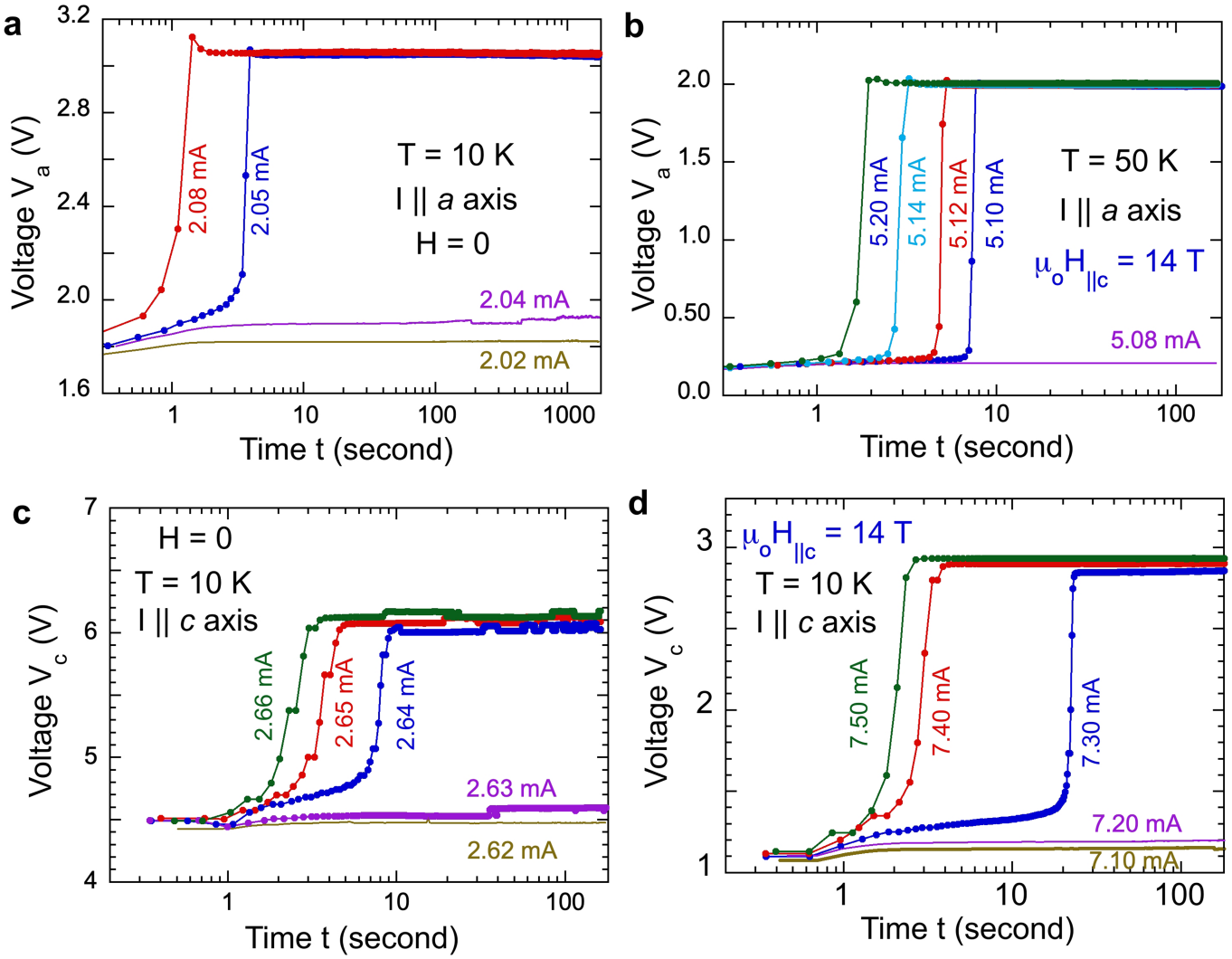

Extended Data Fig. 3 | Additional time-dependent bistable switching data. a, Time-dependent bistable switching at 10 K with 1,800 s elapsed. **b**, Time-dependent bistable switching at 50 K and $\mu_o H_{\|c} = 14$ T. **c**, **d**, Time-dependent bistable switching for $I \| c$ axis at 10 K for $H = 0$ (**c**) and $\mu_o H = 14$ T (**d**).

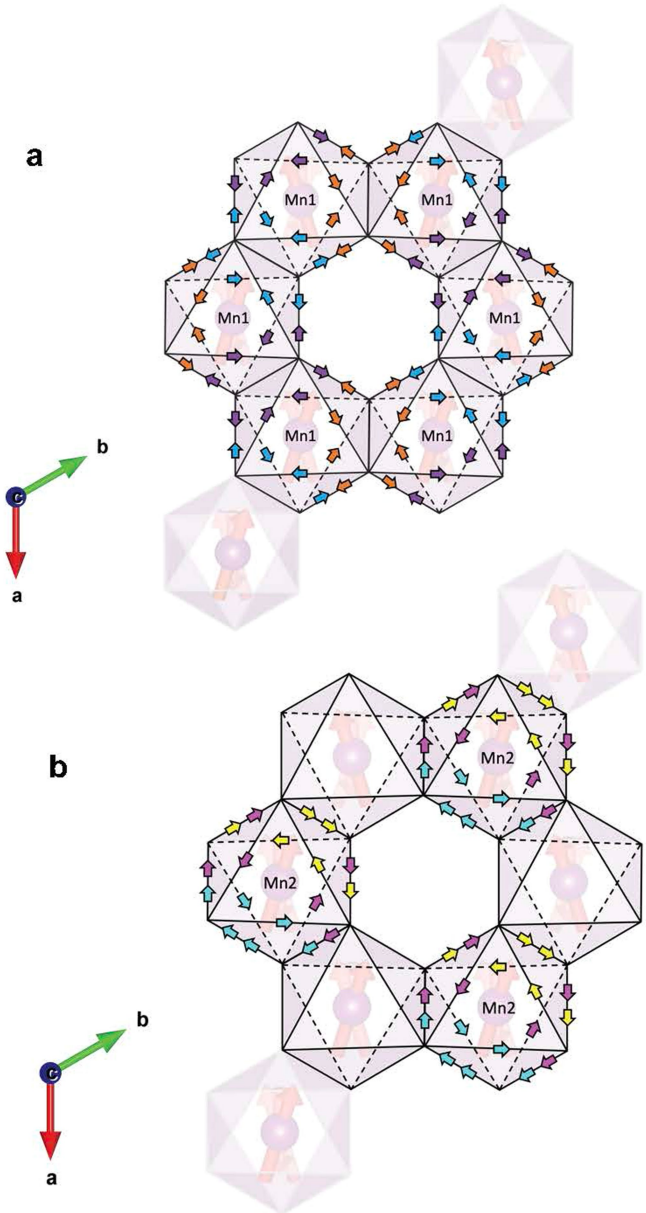

Extended Data Fig. 4 | Chiral orbital current parameters of Ψ_a in the Mn1 (a) and Mn2 (b) planes. a, Three independent currents (orange, purple, and cerulean) run along Te-Te bonds in the Mn1 plane and are symmetry allowed magnetic space group. **b**, Three more independent currents (cyan, magenta, and yellow) run along Te-Te bonds in the Mn2 plane. These currents are not linearly independent of the COC of Fig. 4g in the main text. The sum of the orange, purple, and cerulean COC in **a** gives rise to the difference of the red and blue COC of Fig. 4g in the main text. Moreover, the sum of the cyan, magenta, and yellow COC in **b** gives the difference of the blue and twice purple COC of Fig. 4g. Bonds with two arrows of the same colour indicate that the current magnitude is doubled on that edge. In total, the COC state is parametrized by eight independent loop currents.